PAPER

Vertically stacked GaN/WX$_2$ (X = S, Se, Te) heterostructures for photocatalysts and photoelectronic devices

Dahua Ren, [ID] *[ab] Yunhai Li[b] and Wenqi Xiong [ID] [b]

Tremendous attention has been paid to vertically stacked heterostructures owing to their tunable electronic structures and outstanding optical properties. In this work, we explore the structural, electronic and optical properties of vertically stacked GaN/WX$_2$ (X = S, Se, Te) heterostructures using density functional theory. We find that these stacking heterostructures are all semiconductors with direct band gaps of 1.473 eV (GaN/WTe$_2$), 2.102 eV (GaN/WSe$_2$) and 1.993 eV (GaN/WS$_2$). Interestingly, the GaN/WS$_2$ heterostructure exhibits a type-II band alignment, while the other two stackings of GaN/WSe$_2$ and GaN/WTe$_2$ heterostructures have type-I band alignment. The optical absorption of GaN/WX$_2$ heterostructures is very efficient in the visible light spectrum. Our results suggest that GaN/WX$_2$ heterostructures are promising candidates for photocatalytic water splitting and photoelectronic devices in visible light.

Introduction

Van der Waals (vdW) heterostructures (HS) are used to design unusual electronic devices because of their peculiar physical properties and immense performances.[1] Additionally, vertically stacked heterostructures have innovative applications in electronic devices, such as ultrathin photodetectors,[2] solar cells,[3] memory devices,[4] flexible sensors and transistors[5,6] *etc.* Specifically, two-dimensional (2D) vdW heterostructures with type-II band alignments have promising potential in photovoltaics devices and photocatalysts[7–11] due to their fascinating electronic and optical properties. In type-II heterostructures, the photogenerated holes and electrons become spatially located in different layers. As a result, the recombination of carriers can be effectively prevented and the light energy utilization is significantly enhanced.[12] Moreover, 2D WX$_2$ (X = S, Se, Te) is a typical layered transition metal dichalcogenide family, which has a direct band gap from 1.0 eV to 2.4 eV.[13–22] Among the transition metal dichalcogenides (TMD) materials, monolayer WS$_2$, WSe$_2$, and 1H WTe$_2$ are typically semiconductors with direct band gaps of 2.38 eV,[18,19] 2.11 eV,[20,21] 1.46 eV.[22]

Motivated by 2D graphene-like planar honeycomb structures, 2D group III–V compound semiconductors with planar hexagonal structures have been predicted to be stable.[23–26] In particular, the monolayer hexagonal structure of gallium nitride (GaN) has recently received growing attractions, which has been directly experimentally synthesized *via* graphene encapsulation.[25] Onen *et al.* reported that the indirect band gap of 2D GaN

is 3.42 eV with HSE06 calculation,[26] but the indirect bandgap hindered the practical applications in optoelectronics. In addition, heterostructures based on 2D GaN, such as GaN/blueP, GaN/MoS$_2$, GaN/MoSe$_2$, GaN/WS$_2$, MoSe$_2$/blueP, GaN/ZnO and GaN/BP heterostructures, are able to be formed to type-II band structures, which show good electronic and optical behaviors in photocatalyst and optoelectronic applications.[27–32]

It is also worth to note that 2D WX$_2$, together with 2D GaN, can form vdW heterostructures for their similar structures and same lattice constants. Generally, the superior structures and excellent properties of GaN/WX$_2$ (X = S, Se, Te) heterostructures are significantly valuable to explore, which could potentially provide a platform for applications in photocatalyst and optoelectronic devices.

Computational methods

Ab initio calculations were performed within the framework of density functional theory (DFT),[33,34] as implemented in the Vienna *Ab Initio* Simulations Package (VASP).[35] Electronic exchange and correlation effects were described with the Perdew–Burke–Ernzerhof (PBE)[36] functional of generalized gradient approximation (GGA)[37] and HSE06 hybrid function.[38] Electron–ion interaction were treated with the projector augmented wave (PAW) method,[39,40] with an energy cutoff of 550 eV. And Brillouin zone sampling of K-mesh was set to $9 \times 9 \times 1$ for relaxation. Subsequently, K-mesh points for density of states (DOS) and energy band structures were set to $13 \times 13 \times 1$ and the energy criteria were set as 10^{-5} eV until the residual force was smaller than 10^{-3} eV Å^{-1}. Especially, the vacuum layer thickness was set more than 25 Å to avoid spurious interactions in the neighboring images. As the long-range vdW interaction is

[a]School of Information Engineering, Hubei Minzu University, Enshi, 44500, China. E-mail: rdh_perfect@163.com

[b]Science of Physics and Technology, Wuhan University, Wuhan, 430072, China

important to hold the 2D heterostructure together, the vdW-D3 approach[41] was used to describe long-range electron correlation effects.

The optical properties of 2D GaN/WX$_2$ heterostructures are described by the complex dielectric function $\varepsilon(\omega) = \varepsilon_1(\omega) + i\varepsilon_2(\omega)$, where $\varepsilon_1(\omega)$ and $\varepsilon_2(\omega)$ are real and imaginary parts, respectively. At the same time, the imaginary part is calculated by summing up all possible transitions from the occupied to unoccupied states, which is closely related to the band structure in the absorption behaviors.[42] The imaginary part is given by:

$$\varepsilon_2(\hbar\omega) = \left(\frac{4\pi^2 e^2}{m\omega^2}\right) \sum_{i,j} \int_k \langle i|M|j\rangle^2 f_i\left(1 - f_i^i\right) \times \delta\left(E_{j,k} - E_{i,k} - \omega\right) d^3k$$

(1)

where e, m and ω are the charge, mass of free electrons, and the frequency of incident photons, respectively. Meanwhile, M, i, j and f_i are the dipole momentum, indices of initial and final states, and the Fermi–Dirac distribution function for ith state with wave vector $\mathbf{k}$, respectively. The real part $\varepsilon_1(\omega)$ is obtained from the imaginary $\varepsilon_2(\omega)$ by Kramers–Kronig relation:[43,44]

$$\varepsilon_1(\omega) = 1 + \frac{2}{\pi} P \int_0^\infty \frac{\omega' \varepsilon_2(\omega') d\omega'}{\left(\omega'^2 - \omega^2\right)}$$

(2)

where P is the principal value. Absorption coefficient is then obtained as:[43,44]

$$\alpha(\omega) = \frac{\sqrt{2}\omega}{c}\left[\sqrt{\varepsilon_1^2(\omega) + \varepsilon_2^2(\omega)} - \omega_1(\omega)\right]^{1/2}$$

(3)

Results and discussion

Stability and structures

Stacking patterns can modulate the electronic properties of the vdW heterostructures. Therefore, four typical stacking configurations (AA, AB, AC, AD) have been constructed. In the AA stacking, the Ga atom sits on the top of S/Se/Te atom, while the N atom is on top of W atom. In the AB stacking, the Ga atom is placed on the top of W atom, while the N atom is on the center of the hexagonal site. In the AC stacking, the N atom sits on the top of W atom, while the Ga atom is located on the center of the hexagonal site. In the AD stacking, the Ga atom sits on the top of W atom, while the N atom is on top of S/Se/Te atom. These relaxed structures are shown in Fig. 1. For GaN/WS$_2$ heterostructure, the interface binding energies of AA, AB, AC and AD stacking patterns are -27.72 meV Å^{-2}, -27.01 meV Å^{-2}, -26.69 meV Å^{-2}, and -22.58 meV Å^{-2} respectively. In consistence with other reports,[27,28] after relaxation, AA stacking of GaN/WX$_2$ heterostructures are the most stable due to the lowest interface binding energies. AA stacking patterns are only taken into consideration in the next calculation. The equilibrium lattice constants $a(b)$, bond lengths, bond angles of GaN monolayer, WX$_2$ monolayer and AA stacking GaN/WX$_2$ heterostructures, calculated with GGA–PBE, are listed in Table 1. From Table 1, the calculated lattice constants, bond lengths/angles accord well with previous reports.[13,14,16,23,24,26,28] And the relaxed crystal structures of the GaN, WS$_2$, WSe$_2$, and WTe$_2$ monolayers and GaN/WX$_2$ bilayers are hexagonal. It is clear that the hexagonal unit parameters of GaN/WS$_2$, GaN/WSe$_2$, GaN/WTe$_2$ heterostructures are 3.194 Å, 3.285 Å, 3.388 Å, respectively, which agree well with previous results.[28,29] The lattice mismatches are expressed as $\omega = \frac{|a - c|}{a} \times 100\%$. Where a and c are lattice constants of GaN/WX$_2$ heterostructure and individual WX$_2$ layer or GaN layer. The lattice mismatches of GaN/WS$_2$, GaN/WSe$_2$, GaN/WTe$_2$ heterostructures are 1.7%, 3.0% and 3.4%, meaning that the differences are negligible.

To describe the vdW interactions, the interface binding energies (ΔE) of GaN/WX$_2$ heterostructures are calculated as:

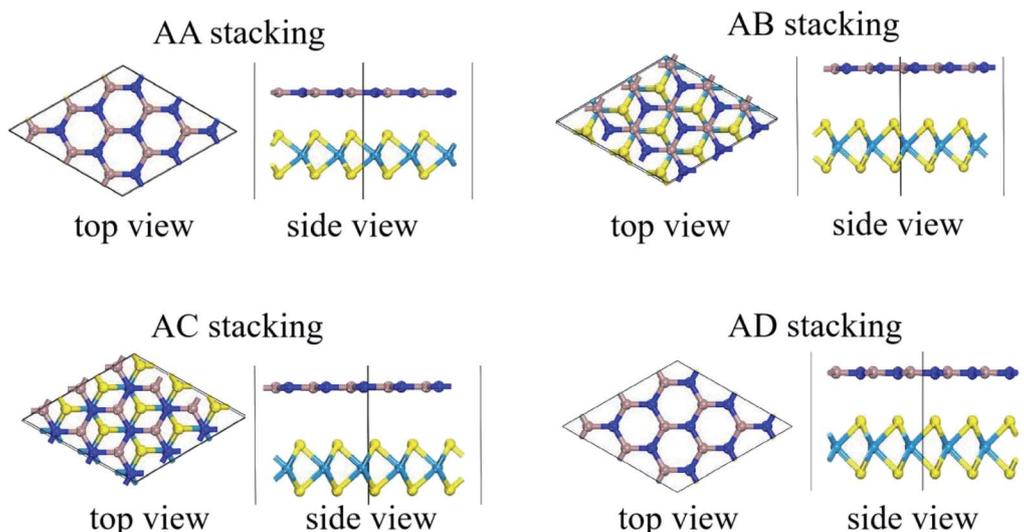$$\Delta E = (E_{HS} - E_{GaN} - E_{WX_2})/S_0$$

(4)

Fig. 1 Relaxed structures of four typical stacking patterns of GaN/WX$_2$ (X = S, Se, Te) heterostructures. Cyan, yellow, dark blue, and brown spheres indicate W, X, N and Ga atoms, respectively.

Table 1 Lattice parameters $a(b)$, bond lengths $l_{X–W}(l_{Ga–N})$, bond angles Θ_{XWX}, interface equilibrium distances d_{eq} and the interface binding energies ΔE were calculated using PBE in comparison to previous theoretical and experimental values

Name		$a\,(b)$/Å	$l_{X–W}$/Å	$l_{Ga–N}$/Å	Θ_{xwx}/°	d_{eq}/Å	ΔE/meV·Å^{-2}
GaN	Theo.	3.21[a], 3.25[b]		1.85[a]	—	—	—
	Cal.	3.248	—	1.858	—	—	—
	Expt.	3.20[c]			—	—	—
WS$_2$	Theo.	3.18[d], 3.14[f]	2.42[d]		81.01[d]	—	—
	Cal.	3.185	2.411	—	81.023	—	—
	Expt.	3.155[e]				—	—
WSe$_2$	Theo.	3.32[d], 3.31[g]	2.55[d]		82.43[d]	—	—
	Cal.	3.295	2.517	—	82.749	—	—
	Expt.	3.286[e]			—	—	—
WTe$_2$	Theo.	3.51[g]			—	—	—
	Cal.	3.502	2.736	—	83.334	—	—
GaN/WS$_2$	Theo.	3.200[f]	2.433[f]	1.852[h]	—	3.479[f]	−33.36[f], −19.61[h]
	Cal.	3.194	2.431	1.845	81.144	3.081	−27.72
GaN/WSe$_2$	Theo.	3.29[h]	—	—	—	—	−21.87[h]
	Cal.	3.285	2.543	1.897	82.417	3.139	−28.05
GaN/WTe$_2$	Cal.	3.388	2.810	1.906	83.799	3.236	−37.63

[a] Ref. 26. [b] Ref. 23. [c] Ref. 25. [d] Ref. 16. [e] Ref. 14. [f] Ref. 28. [g] Ref. 13. [h] Ref. 29.

where ΔE refers to the interface binding energies at the interface of GaN/WX$_2$ heterostructures, and E_{HS}, E_{GaN}, E_{WX_2}, S_0 represent the total energies of heterostructures, GaN monolayer, WX$_2$ monolayer, the interface areas of the heterostructures, respectively. The interface areas of the heterostructures are calculated by multiplying $\boldsymbol{a}$ and $\boldsymbol{b}$ vectors in hexagonal unit cells. Then, the interface binding energies of GaN/WX$_2$ heterostructures are listed in Table 1, consistent with other theoretical reports.[28,29] As is shown in Fig. 2, the optimal distances between N atom in the GaN layer and X atom in the WX$_2$ layer are 3.081 Å, 3.139 Å, 3.236 Å, respectively, indicating that no bonds between Ga and X atoms are formed and all these heterostructures are formed by the same magnitude order of van der Waals (vdW) forces as others, such as GaN–blueP,[27] GaN/WS$_2$,[28] GaN/BP[30] and typical vdW graphite.[45]

Obviously, the interface binding energies of GaN/WS$_2$, GaN/WSe$_2$ and GaN/WTe$_2$ heterostructures are −27.72, −28.05, and −37.63 meV Å^{-2}, demonstrating that the interactions between two layers belong to physically vdW forces. All the interface binding energies are negative, suggesting that the GaN/WX$_2$ heterostructures have favorable energies during the formation.

Electronic properties

In the following section, projection-resolved band structures of GaN/WX$_2$ heterostructures are depicted in Fig. 3. All the GaN/WX$_2$ heterostructures are direct band gap semiconductors. Both the valence band maximum (VBM) and the conduction band minimum (CBM) of the GaN/WX$_2$ (X = S, Se, Te) heterostructures locate at the K point of Brillouin zone (BZ). The band gaps of GaN/WS$_2$, GaN/WSe$_2$, GaN/WTe$_2$ heterostructures are 1.993 eV, 2.102 eV, 1.473 eV, smaller than both individual GaN (3.241 eV) layer and individual WS$_2$ (2.357 eV), WSe$_2$ (2.119 eV), WTe$_2$ (1.594 eV) layer according to HSE06 calculations, which agrees well with the theoretical values of GaN (3.23 eV),[23] WTe$_2$ (1.49 eV)[22] and experimental values of WS$_2$ (2.38 eV),[5] WSe$_2$

(2.11 eV).[8] Specially, GaN/WS$_2$ heterostructure has a type II band alignment, which is beneficial to the separation of the photo-generated holes and electrons in different layers, the prevention of the recombination of carriers, and the enhancement of the light energy utilization. It is also found that the GaN/WSe$_2$ and GaN/WTe$_2$ heterostructures have type-I band alignment semi-conductors for both the VBM and CBM of GaN/WSe$_2$ and GaN/WTe$_2$ heterostructures come from the W-dz^2 orbitals of the WSe$_2$ and WTe$_2$ layer, which can be used in light emitting diodes (LED),[46] indicating that the interlayer interactions between the GaN layer and the WX$_2$ (X = Se, Te) layer reduce the band gap values. Therefore, the band gaps of the GaN/WX$_2$ heterostructures could be significantly changed by vertically stacked heterostructures, which could provide a good opportunity to work on band engineering and electronic device
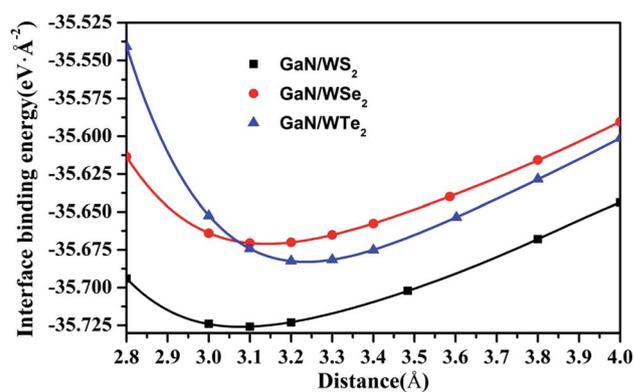
Fig. 2 Plot of interface binding energies as function of interlayer distances for GaN/WS$_2$, GaN/WSe$_2$, and GaN/WTe$_2$ heterostructures. 5th order polynomial has been employed for fitting. In order to clarify the equilibrium distances between the GaN layer and WX$_2$ layer, the values of interface binding energies of both the GaN/WSe$_2$ and GaN/WTe$_2$ heterostructures are shifted downwards by 1.80 eV, 5.40 eV, respectively.
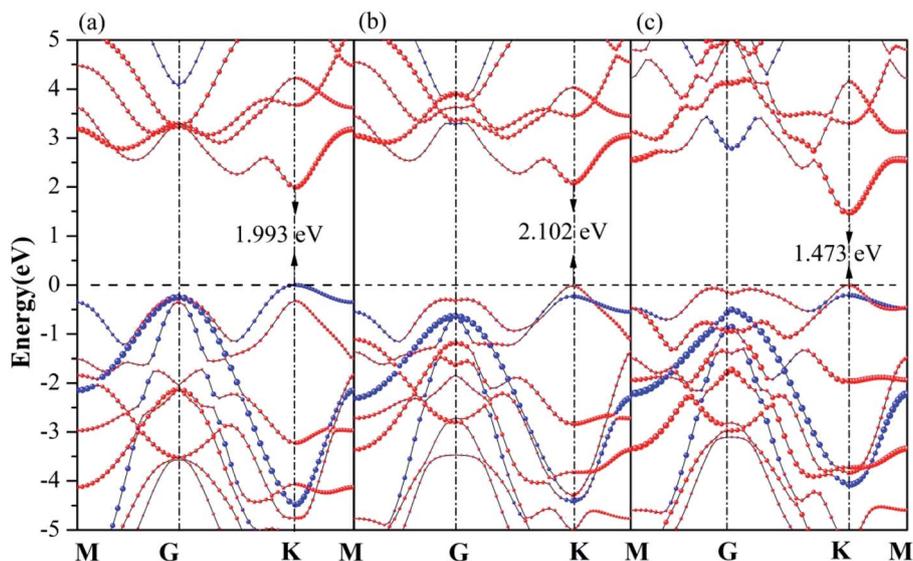
Fig. 3 Projection-resolved band structures of (a) GaN/WS₂, (b) GaN/WSe₂, and (c) GaN/WTe₂ heterostructures. Blue and red lines indicate contributions from GaN and WX₂ layer, respectively.

designs. It is interesting that the band gap of GaN/WS₂ heterostructure is larger than the minimum required energy of the photocatalytic reaction (1.23 eV), which is potential for a photocatalyst in water splitting.

As reflected in the projection-resolved band structures, the band gap of WX_2 monolayer is decreased by the downshift of CBM as well as the upshift of VBM at K point. The contribution of VBM of GaN/WS₂ heterostructure is GaN layer and that of CBM is WS₂ layer. In Fig. 4(a), the blue and red lines present the DOS of GaN and WS₂ layer in GaN/WS₂ heterostructure. Both the contributions of VBM and CBM of GaN/WSe₂ and GaN/WTe₂ heterostructures are derived from WSe₂ and WTe₂ layer, as shown in Fig. 4(b and c). Obviously, for GaN/WS₂ heterostructure, the VBM and CBM are respectively confined in GaN and WS₂ layer, which also demonstrates that GaN/WS₂ heterostructure has a type-II band alignment.

Photocatalyst and optoelectronic performances

The absorption coefficients of GaN/WX₂ heterostructures are calculated, as illustrated in Fig. 5(a). It is clear that the first peaks in absorption spectrum of GaN/WS₂, GaN/WSe₂, GaN/WTe₂ heterostructures locate at 3.03, 2.69, 2.25 eV, which are mainly contributed by WX₂ layers. The absorption spectrum of GaN/WX₂ heterostructures covers the whole incident solar spectrum,[47] which makes well suitable applications for optoelectronic devices in visible light.

A schematic plot of migrating carriers to depict the dynamic processes of photogenerated carriers at the GaN/WS₂ interface is shown in Fig. 5(b). In the GaN/WS₂ heterostructure, the photogenerated electrons start to transfer from the GaN layer the WS₂ layer in the conduction band, which is motivated by the conduction band offset (CBO) (0.71 eV). Meanwhile, the
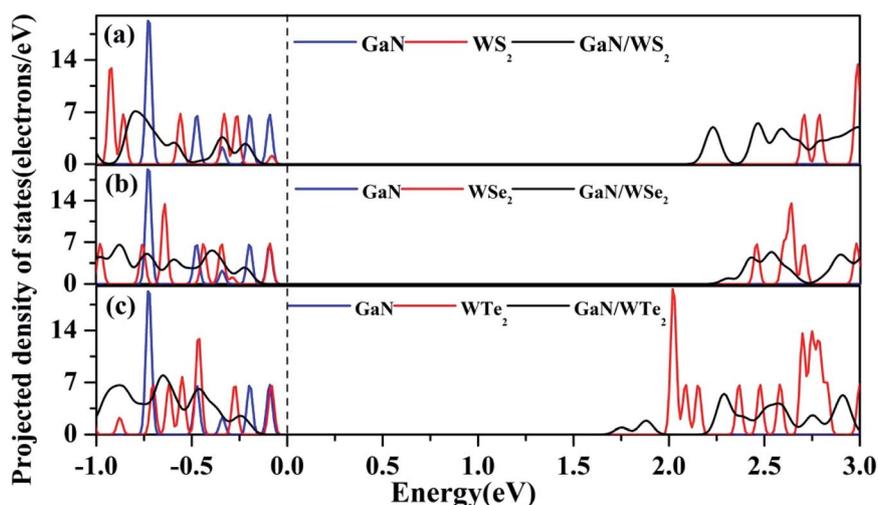

Fig. 4 Projected density of states (PDOS) of (a) GaN/WS₂, (b) GaN/WSe₂, and (c) GaN/WTe₂ heterostructures. Fermi level is set to zero as indicated by the black dashed line.
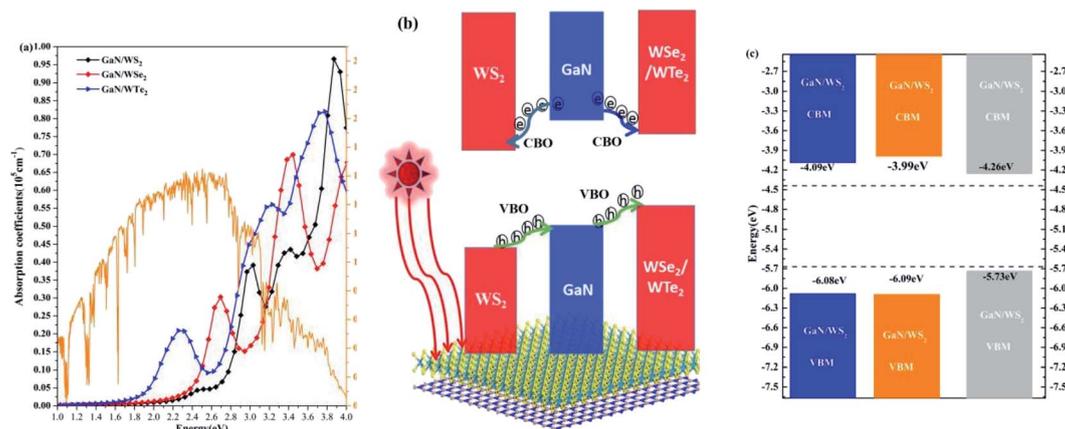
Fig. 5 (a) Absorption spectrum of GaN/WS$_2$, GaN/WSe$_2$, and GaN/WTe$_2$ heterostructures. Incident AM 1.5 G solar flux[48] is plotted in orange solid line. (b) Schematic plot of the migration of photogenerated electrons and holes at the GaN/WS$_2$ interface. (c) Band-edge alignments of GaN/WX$_2$ heterostructures.

photogenerated holes in the valence band move from the WS$_2$ layer to the GaN layer, which are driven by a large valence band offset (VBO) (1.60 eV). Hence, the GaN/WS$_2$ heterostructure, owing a type-II band alignment, could be utilized as a photocatalyst. As for the GaN/WSe$_2$ and GaN/WTe$_2$ heterostructures, one can see that all the photogenerated carriers of the GaN layer are likely to move to the WSe$_2$ (WTe$_2$) layer. The VBO and CBO between GaN and WSe$_2$ (WTe$_2$) layers are 1.98 eV (2.97 eV) and 0.86 eV (1.72 eV), respectively. As a result, the photogenerated carriers can be located in the WSe$_2$ (WTe$_2$) layers to build light-emitting diodes (LEDs).[46] The band edge positions of GaN/WS$_2$, GaN/WSe$_2$, GaN/WTe$_2$ heterostructures are illustrated in Fig. 5(c). The CBMs of GaN/WS$_2$, GaN/WSe$_2$, GaN/WTe$_2$ heterostructures are −4.09, −3.99, −4.26 eV, respectively, whereas the VBMs of GaN/WS$_2$, GaN/WSe$_2$, GaN/WTe$_2$ heterostructures are −6.08, −6.09, −5.73 eV, respectively. Those are within the oxidation potential (E_{O_2/H_2O}, −5.67 eV) of water and the reduction potential (E_{H^+/H_2}, −4.44 eV). Especially, the redox reaction in the GaN/WS$_2$ heterostructure occurs in different layers: water oxidation occurs in the GaN layer, meanwhile water reduction takes place in the WS$_2$ layer.

It is well known that the lifetime of photogenerated carriers is significantly influenced by the build-in electric field. Hence, build-in electric field induced by ground state charge transfer were investigated. Based on Bader charge analysis,[48] the charge transfer from the GaN layer to the WS$_2$ layer is 0.029e, leading to an electric field pointing to GaN from WS$_2$. This electric field will promote the migration of electrons from the GaN layer to WS$_2$ layer and holes from the WS$_2$ layer to GaN layer. The build-in electric field $E = P/\varepsilon_0\varepsilon_r S_0 d_{eq}$ of 3.69×10^9 V m^{-1} is acquired in the junction region of GaN/WS$_2$ heterostructure. Where $P = \Delta q \cdot d_{eq} = 0.089e \cdot$Å is the size of dipole moment, $\varepsilon_0 = 8.850 \times 10^{-12}$ F m^{-1} refers to the permittivity of free space, $\varepsilon_r = 1$ represents the relative dielectric constant, $S_0 = 8.835 \times 10^{-20}$ m^2 is the interfaces area of the WS$_2$/GaN heterostructure, $d_{eq} = 3.081 \times 10^{-10}$ m denotes the interlayer equivalent distance.

Conclusions

In summary, the electronic and optical properties of GaN/WX$_2$ heterostructures have been performed within density functional theory. It is found that all the hexagonal GaN/WX$_2$ heterostructures are stable semiconductors with direct band gaps. Interestingly, among them, the GaN/WS$_2$ heterostructure has a type-II band alignment, which is beneficial in photocatalysts for water splitting. However, both the GaN/WSe$_2$ and GaN/WTe$_2$ heterostructures exhibit type-I band alignment, which can be utilized in LED. In the GaN/WS$_2$ heterostructure, the charge transport from the GaN layer to the WS$_2$ layer is 0.029e, based on Bader charge analysis, forming a build-in electric field favorable for charge separation. The build-in electric field $E = P/\varepsilon_0\varepsilon_r S_0 d_{eq}$ of 3.69×10^9 V m^{-1} is acquired in the junction region of GaN/WS$_2$ heterostructure. The absorption behaviors of GaN/WX$_2$ heterostructures are also performed, and results show that GaN/WX$_2$ heterostructures are very efficient at absorbing the visible light to expand the application to photocatalyst and photoelectronic devices.

Conflicts of interest

There are no conflicts to declare.

Acknowledgements

References

1 A. Geim and I. Grigorieva, *Nature*, 2013, **499**, 419–425.
2 M. Massicotte, P. Schmidt, F. Vialla, K. G. Schädler, P. A. Reserbat, K. Watanabe, T. Taniguchi, K. J. Tielrooij and F. H. L. Koppens, *Nat. Nanotechnol.*, 2015, **11**(1), 42–46.

3 C. H. Lee, G. H. Lee, A. M. van der Zande, W. Chen, Y. Li, M. Han, X. Cui, G. Arefe, C. Nuckolls, T. F. Heinz, J. Guo, J. Hone and P. Kim, *Nat. Nanotechnol.*, 2014, **9**(9), 676–681.

4 L. Britnell, R. V. Gorbachev, R. Jalil, B. D. Belle, F. Schedin, A. Mishchenko, T. Georgiou, M. I. Katsnelson, L. Eaves, S. V. Morozov, N. M. R. Peres, J. Leist, A. K. Geim, K. S. Novoselov and L. A. Ponomarenko, *Science*, 2012, **335**(6071), 947–950.

5 H. Wang, H. Yuan, H. S. Sae, Y. Li and Y. Cui, *Chem. Soc. Rev.*, 2015, **44**(9), 2664–2680.

6 N. Lu, H. Guo, L. Li, J. Dai, L. Wang, W. N. Mei, X. Wu and X. C. Zeng, *Nanoscale*, 2014, **6**(5), 2879–2886.

7 Z. Y. Zhu, K. Ren, H. B. Shu, Z. Cui, Z. M. Huang, J. Yu and Y. J. Xu, *Catalyst*, 2021, **11**(8), 991.

8 Y. C. Fan, X. K. Ma, X. B. Liu, J. R. Wang, H. Q. Ai and M. W. Zhao, *J. Phys. Chem. C*, 2018, **122**(49), 27803–27810.

9 J. B. Lou, K. Ren, Z. M. Huang, W. Y. Huo, Z. Y. Zhu and J. Yu, *RSC Adv.*, 2021, **11**(47), 29576–29584.

10 K. Ren, R. X. Zheng, P. Xu, D. Cheng, W. Y. Huo, J. Yu, Z. R. Zhang and Q. Y. Sun, *Nanomaterials*, 2021, **11**(9), 2236.

11 J. Linghu, T. Yang, Y. Luo, M. Yang, J. Zhou, L. Shen and Y. P. Feng, *ACS Appl. Mater. Interfaces*, 2018, **10**(38), 32142–32150.

12 B. Peng, G. Yu, X. Liu, B. Liu, X. Liang, L. Bi, L. Deng, T. C. Sum and K. P. Loh, *2D Mater.*, 2016, **3**(2), 025020.

13 A. Kumara and P. K. Ahluwalia, *Eur. Phys. J. B*, 2012, **85**, 186.

14 W. S. Yun, S. W. Han, S. C. Hong, I. G. Kim and J. D. Lee, *Phys. Rev. B: Condens. Matter Mater. Phys.*, 2012, **85**(3), 033305.

15 H. Shu, Y. Tong and J. Guo, *Phys. Chem. Chem. Phys.*, 2017, **19**(16), 10644–10650.

16 C. H. Chang, *Phys. Rev. B: Condens. Matter Mater. Phys.*, 2013, **88**, 195420.

17 B. J. Wang, X. H. Li, R. Zhao, X. L. Cai, W. Y. Yu, W. B. Li, Z. S. Liu, L. W. Zhang and S. H. Ke, *J. Mater. Chem. A*, 2018, **6**(19), 8923–8929.

18 H. M. Hill, A. F. Rigosi, K. T. Rim, G. W Flynn and T. F. Heinz, *Nano Lett.*, 2016, **16**, 4831–4837.

19 A. F. Rigosi, H. M. Hill, Y. Li, A. Chernikov and T. F. Heinz, *Nano Lett.*, 2015, **15**(8), 5033–5038.

20 S. Y. Gao, L. Yang and C. D. Spataru, *Nano Lett.*, 2017, **17**, 7809–7813.

21 S. Park, N. Mutz, T. Schultz, S. Blumstengel, A. Han, A. Aljarb, L. J. Li, E. J. W. List-Kratochvil, P. Amsalem and N. Koch, *2D Mater.*, 2018, **5**, 025003.

22 V. Wang, Y. Y. Liang, Y. Kawazeo and W. T. Geng, 2018, arXiv:1806.04285.

23 H. L. Zhuang, A. K. Singh and R. G. Hennig, *Phys. Rev. B: Condens. Matter Mater. Phys.*, 2013, **87**(16), 165415.

24 H. B. Shu, X. H. Niu and X. J. Ding, *Appl. Surf. Sci.*, 2019, **479**, 475–481.

25 Z. Y. Al Balushi, K. Wang, R. K. Ghosh, R. A. Vila, S. M. Eichfeld, J. D. Caldwell, X. Qin, Y. C. Lin, P. A. DeSario, G. Stone, S. Subramanian, D. F. Paul, R. M. Wallace, S. Datta, J. M. Redwing and J. A. Robinson, *Nat. Mater.*, 2016, **15**, 1166.

26 A. Onen, D. Kecik, E. Durgun and S. Ciraci, *Phys. Rev. B: Condens. Matter Mater. Phys.*, 2016, **93**, 085431.

27 M. L. Sun, J. P. Chou, J. Yu and W. C. Tang, *Phys. Chem. Chem. Phys.*, 2017, **19**, 17324.

28 H. B. Shu, *Mater. Sci. Eng., B*, 2020, **261**, 114672.

29 Z. Cui, K. Ren, Y. M. Zhao, X. Wang, H. B. Shu, J. Yu, W. C. Tang and M. L. Sun, *Appl. Surf. Sci.*, 2019, **492**, 513–519.

30 H. B. Shu, M. L. Zhao and M. L. Sun, *ACS Appl. Nano Mater.*, 2019, **2**, 6482–6491.

31 H. B. Shu, Y. Yang and M. L. Sun, *Phys. Chem. Chem. Phys.*, 2019, **21**, 15760.

32 H. B. Shu, *Mater. Adv.*, 2020, **1**, 1849.

33 P. Hohenberg and W. Kohn, *Phys. Rev.*, 1964, **136**, B864.

34 B. Y. Tong and L. J. Sham, *Phys. Rev.*, 1966, **144**(1), 1–4.

35 G. Kresse and J. Hafner, *Phys. Rev. B: Condens. Matter Mater. Phys.*, 1993, **47**, 558–561.

36 J. P. Perdew, J. P. Burke and M. Ernzerhof, *Phys. Rev. Lett.*, 1996, **77**, 3865–3868.

37 K. Burke, J. P. Perdew and M. Ernzerhof, *Int. J. Quantum Chem.*, 1997, **61**, 287–293.

38 J. Heyd, G. E. Scuseria and M. Ernzerhof, *J. Chem. Phys.*, 2003, **118**, 8207–8215.

39 G. Kresse and D. Joubert, *Phys. Rev. B: Condens. Matter Mater. Phys.*, 1999, **59**, 1758–1775.

40 P. E. Blöchl, *Phys. Rev. B: Condens. Matter Mater. Phys.*, 1994, **50**, 17953–17979.

41 S. Grimme, J. Antony, S. Ehrlich and H. Krieg, *J. Chem. Phys.*, 2010, **132**, 154104.

42 M. Gajdoš, K. Hummer, G. Kresse, J. Furthmüller and F. Bechstedt, *Phys. Rev. B: Condens. Matter Mater. Phys.*, 2006, **73**, 045112.

43 S. L. Adler, *Phys. Rev.*, 1962, **126**, 413–420.

44 H. Komsa and A. V. Krasheninnikov, *Phys. Rev. B: Condens. Matter Mater. Phys.*, 2013, **88**, 085318.

45 X. Chen, F. Tian, C. Persson, W. Duan and N. X. Chen, *Sci. Rep.*, 2013, **3**, 3046.

46 S. Nakamura, M. Senoh, N. Iwasa and S. I. Nagahama, *Jpn. J. Appl. Phys.*, 1995, **34**, L797.

47 The AM 1.5 G Spectrum was taken from the NREL website: https://Rredc.Nrel.Gov/Solar/Spectra/Am1.5 and integrated with the trapezoid rule.

48 E. Sanville, S. D. Kenny, R. Smith and G. Henkelman, *J. Comput. Chem.*, 2007, **28**, 899–908.